13. Tolman, R. C. J. The effect of droplet size on surface tension. *J. Chem. Phys.* **17**, 333–337 (1949).

14. van Giessen, A. E., Blokhuis, E. M. & Bukman, D. J. Mean field curvature corrections to the surface tension. *J. Chem. Phys.* **108**, 1148–1156 (1998).

15. Meunier, J. Liquid interfaces: role of the fluctuations and analysis of ellipsometry and reflectivity measurements. *J. Phys.* **48**, 1819–1831 (1987).

16. Braslau, A. *et al.* Surface roughness of water measured by x-ray reflectivity. *Phys. Rev. Lett.* **54**, 114–117 (1985).

17. Rice, S. A. X-ray reflection from liquids. *Nature* **316**, 108 (1985).

18. Daillant, J., Bosio, L., Harzallah, B. & Benattar, J. J. Structural properties and elasticity of amphiphilics on water. *J. Phys.* II **1**, 149–170 (1991).

19. Sinha, S. K., Sirota, E. B. & Garoff, S. X-ray and neutron scattering from rough surfaces. *Phys. Rev.* B **38**, 2297–2311 (1988).

20. Daillant, J. & Bélorgey, O. Surface scattering of x-rays in thin films. i. Theoretical treatment. *J. Chem. Phys.* **97**, 5824–5836 (1992).

21. Dietrich, S. & Haase, A. Scattering of x-rays and neutrons at interfaces. *Phys. Rep.* **260**, 1–138 (1995).

22. Fukuto, M. *et al.* X-ray measurements of noncapillary spatial fluctuations from a liquid surface. *Phys. Rev. Lett.* **81**, 3455–3458 (1998).

23. Tostmann, H. *et al.* Surface structure of liquid metals and the effect of capillary waves: x-ray studies on liquid indium. *Phys. Rev.* B **59**, 783–791 (1999).

24. Gourier, C. *et al.* Bending energy of amphiphilic films at the nanometer scale. *Phys. Rev. Lett.* **78**, 3157–3160 (1997).

25. Napiórkowski, M. & Dietrich, S. Structure of the effective hamiltonian for liquid-vapor interfaces. *Phys. Rev.* A **47**, 1836–1849 (1993).

26. Stecki, J. Extended capillary wave theory and the ellipsometric coefficient. *J. Chem. Phys.* **109**, 5002–5007 (1998).

27. Magli, R., Barocchi, F., Chieux, P. & Fontana, R. Experimental determination of the long-range potential of argon pairs by means of small-angle neutron scattering. *Phys. Rev. Lett.* **77**, 846–848 (1996).

Electrically induced structure formation and pattern transfer

Erik Schäffer*, **Thomas Thurn-Albrecht**†, **Thomas P. Russell**† **& Ullrich Steiner***‡

* *Fakultät für Physik, Universität Konstanz, 78457 Konstanz, Germany*
† *Polymer Science and Engineering Department, University of Massachusetts at Amherst, Amherst, Massachusetts 01003, USA*
‡ *Department of Polymer Chemistry, University of Groningen, Nijenborgh 4, 9747 AG Groningen, The Netherlands*

The wavelength of light represents a fundamental technological barrier[1] to the production of increasingly smaller features on integrated circuits. New technologies that allow the replication of patterns on scales less than 100 nm need to be developed if increases in computing power are to continue at the present rate[2]. Here we report a simple electrostatic technique that creates and replicates lateral structures in polymer films on a submicrometre length scale. Our method is based on the fact that dielectric media experience a force in an electric field gradient[3]. Strong field gradients can produce forces that overcome the surface tension in thin liquid films, inducing an instability that features a characteristic hexagonal order. In our experiments, pattern formation takes place in polymer films at elevated temperatures, and is fixed by cooling the sample to room temperature. The application of a laterally varying electric field causes the instability to be focused in the direction of the highest electric field. This results in the replication of a topographically structured electrode. We report patterns with lateral dimensions of 140 nm, but the extension of the technique to pattern replication on scales smaller than 100 nm seems feasible.

The interaction of an electric field with matter is well understood[3]. Common experiments demonstrate the forces on dielectric materials in electric fields, such as a dielectric liquid which is drawn into the air gap of a plate capacitor when a voltage is applied across the plates. As electrostatic interactions are relatively strong and long-range, they can be used to control structures on length scales which are difficult to manipulate in any other manner. One challenge in this context is the creation of lateral features below the diffraction limit of light. Various techniques for the manufacture of lithographic layers with submicrometre structures have been proposed, such as particle lithography, lithography using scanning near-field microscopes, and printing or embossing structures onto surfaces[2]. Here we describe a particularly simple addition to this collection of submicrometre replication techniques: the electrostatic transfer of a master pattern into a polymer film. While electric fields have been used before to orient the microphases in block copolymer melts[4–8], the work presented here focuses on the use of electric fields to control and organize polymers laterally to replicate a master pattern.

This work has two main aspects. First, we show that a thin liquid film can be destabilized by strong electric fields, applied across the film by means of two capacitor plates. This instability leads to the formation of ordered lateral structures. We also present a theoretical model describing the destabilization process. Second, we make use of this effect for electrostatic lithography: one of the capacitor plates is used as a topographic master. Patterns down to lateral dimensions of 140 nm have been replicated.

A sketch of the experimental set-up is shown in Fig. 1a. Initially, a thin polymer film of thickness h was spin-coated from solution onto a highly polished silicon wafer serving as one of the electrodes. Subsequently, another silicon wafer was mounted as the opposing electrode at a distance d, leaving a thin air gap. The assembly was then heated above the glass transition temperature of the polymer (T_g), and a small voltage U (20–50 V) was applied. To assure the air gap, the top electrode has a small step. Using a wedge geometry, a range of d values could be achieved, while locally maintaining a nearly parallel electrode configuration. Air gaps varying from 100 nm to 1,000 nm were obtained this way. The voltage and the geometry of the capacitor device determine the electric field. The electrostatic driving force scales with the difference between the electric field in the polymer film, E_p, and the field in the air gap. E_p increases with decreasing values of d, and with increasing polymer film thickness h. The low applied voltage, combined with the small distance between the electrodes ($d < 1\,\mu m$), leads to high electric fields E_p (10^7–10^8 V m^{-1}). During the annealing step, a small current
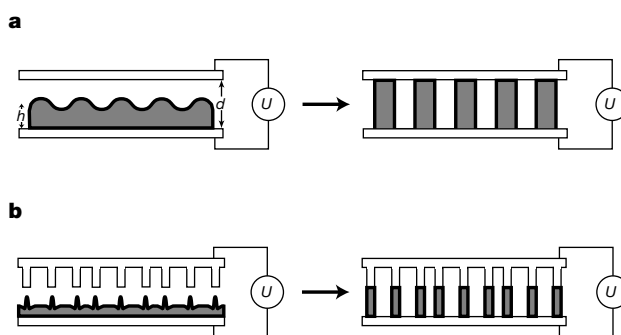
Figure 1 Schematic representation of the capacitor device. **a**, The electrostatic pressure acting at the polymer (grey)–air interface causes an instability in the film (left). This instability has a well defined wavelength. Eventually, polymer columns span the gap between the two electrodes (right). **b**, If the top electrode is replaced by a topographically structured electrode, the instability occurs first at the locations where the distance between the electrodes is smallest (left). This leads to replication of the electrode pattern (right).

874 NATURE | VOL 403 | 24 FEBRUARY 2000 | www.nature.com

was flowing through the device (10–50 mA cm^{-2}). At high electric fields, the current is caused by an ion conduction mechanism mediated by small impurity molecules in the polymer matrix[9]. After an annealing time which ranged from several minutes to a few hours, the polymer was immobilized by quenching below T_g, the top electrode was mechanically removed, and the morphology of the polymer film was investigated by optical microscopy and atomic force microscopy (AFM).

The results of typical experiments are shown in the optical micrographs of Fig. 2. Depending on the electric field strength and the annealing time, we observe either surface undulations (Fig. 2a) or a columnar structure where the liquid bridges the gap between the electrodes (Fig. 2b). As the two electrodes are not perfectly parallel, the electric field exhibits a small lateral variation and we usually observe both situations (Fig. 2a, b) on the same sample. In the case of the columnar phase, the electrode spacing can be measured by the AFM. We emphasize that the structures in Fig. 2 are observed only with the application of a very high electric field ($>10^7$ V m^{-1}). We observed no surface features in the absence of an applied field, in contrast to recent, intriguing results by Chou *et al.*[10,11]. For significantly longer annealing times, dispersive van der Waals interactions will cause the breakup of the film[12]. When the instability is caused by purely dispersive interactions, very different time scales of breakup of the film are observed and the film morphology is typically stochastic and not ordered. This was confirmed by a control experiment without applied voltage (not shown here), in which the film remained stable.

Different degrees of order are evident in Fig. 2. The ordering phenomenon originates from the repulsion of the equally charged undulation maxima and minima. While the film morphology in Fig. 2b exhibits only imperfect order, a more complete hexagonal packing is achieved in Fig. 2c. The main difference between the two images is the initial thickness h of the polymer film (93 and 193 nm, respectively). With otherwise similar parameters, this leads to a more dense lateral arrangement of the polymer columns and to an increased column–column repulsion. As a consequence, improved hexagonal order is observed in Fig. 2c, compared to Fig. 2b.

While nearest-neighbour interactions lead to a hexagonal symmetry, second-order effects can be observed as well, as demonstrated for the nucleated instability in Fig. 2d. The locally higher value of h at the nucleation point leads to a higher electric field and an increased driving force. This causes a depletion of the nearest-neighbour undulations. The next-nearest neighbours, on the other hand, are again amplified. They form a rosette on a circle with a radius $r = 2\lambda$ and a circumference of $2\pi r \approx 12\lambda$, where λ is a characteristic wavelength. Beyond the circle of next-nearest neighbours, the instability decays with increasing distance. In the absence of nucleation effects, a similar argument also explains the hexagonal closest packing of the columns in Fig. 2c, where each maximum is surrounded by six neighbours, corresponding to a circle with radius λ and circumference $\sim 6\lambda$.

We also note the well defined lateral length scale of the surface undulations. The wavelength λ is a function of the electric field E_p, which varies inversely with the electrode spacing. The lateral structure dimensions, as well as the plateau height, are readily measured with the AFM, yielding λ as a function of electrode spacing d. In Fig. 3, λ is plotted as a function of the electric field in the polymer layer, E_p. For a given film thickness h, the characteristic lateral structure size exhibits a power-law dependence on the increasing electric field, corresponding to a decrease in the electrode spacing (top axis).

Theoretically, the origin of the film instability can be understood by considering the balance of forces that act at the polymer–air interface. The surface tension γ minimizes the area of the polymer–air surface, and stabilizes the homogeneous polymer film. The electric field, on the other hand, polarizes the dielectric. This results in an effective displacement charge density at the liquid–air interface, which destabilizes the film. When this balance of forces is written in terms of pressures, an electrostatic pressure p_{el} is opposed by the Laplace pressure. A local perturbation in the film thickness
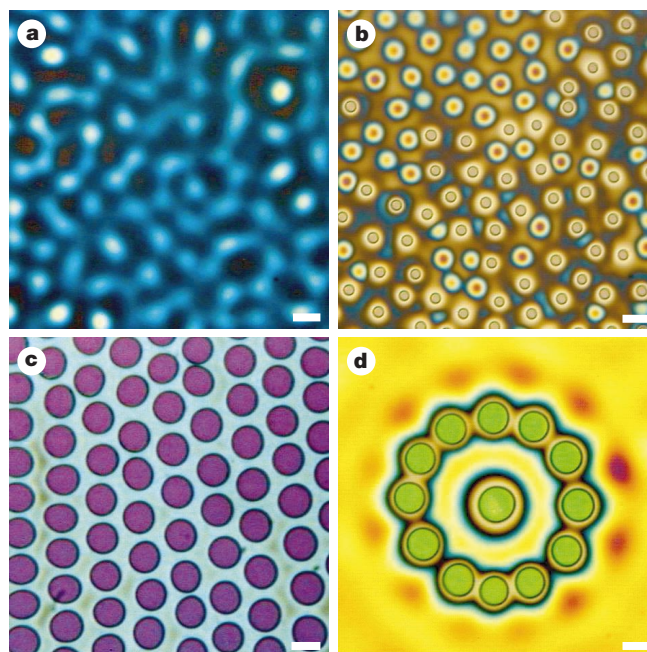
Figure 2 Optical micrographs of polystyrene films which have been exposed to an electric field. In **a** and **b**, a 93-nm-thick polystyrene film was annealed for 18 h at 170 °C with an applied voltage $U = 50$ V. As the electrode spacing in **a** was larger than in **b**, corresponding to a lower electric field E_p, two different stages of the instability were observed, corresponding to Fig. 1a and b. In **c** and **d**, the thickness of the polystyrene film was doubled ($h = 193$ nm). This leads to a denser packing of the polymer columns and to an enhanced repulsion between the columns. As a result, we observe a more complete hexagonal order in **c**. In **d** a second-order effect is observed for a nucleated instability (see text). Instead of a hexagonal symmetry which characterizes the nearest neighbours in **c**, a ring of 12 columns lies on a circle with a radius of 2λ. The scale bars correspond to 10 μm in **a** and **b** and to 5 μm in **c** and **d**. The colours arise from the interference of light, and correspond to the local thickness of the polymer structures (for example, in **d**, yellow corresponds to a film thickness of ~ 200 nm, green to ~ 450 nm).
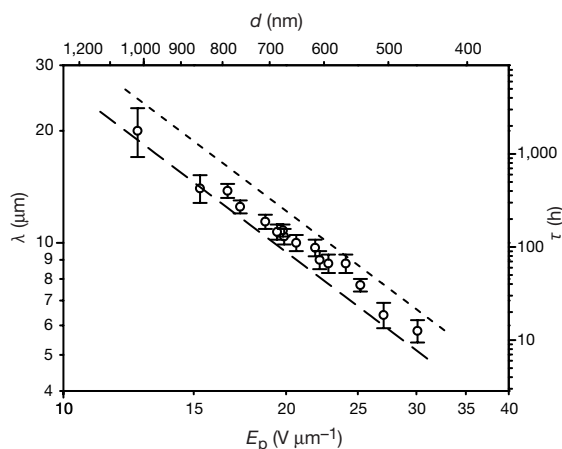
Figure 3 Variation of the lateral wavelength λ as a function of the electric field E_p in the polymer film. The open circles are experimental data for the set-up in Fig. 1a with a 93-nm-thick polystyrene film and an applied voltage of 30 V. The sample was annealed for 120 h at 170 °C. After removal of the top plate, λ and the electrode spacing d were measured by imaging the polymer columns with the AFM. Also plotted are the theoretical predictions from equation (1). The electrostatic pressure is computed as: $p_{el} = -f(\epsilon)E_p^2$. The precise functional dependence $f(\epsilon)$ of p_{el} on the dielectric constant ϵ of the polymer is not known. Two slightly different models yield the dotted and dashed lines which bound the experimental data. The right-hand axis indicates the predicted time constant τ for the pattern-formation process corresponding to the dashed line.

results in a pressure gradient which drives a flow of the dielectric liquid in the plane of the film. The liquid flow next to a solid surface is given by a formula of the Poiseuille type[13] which, together with a mass-conservation equation, establishes a differential equation describing the temporal response of the liquid. A common approach to the investigation of the effect of external forces on a liquid film is a linear stability analysis. A small sinusoidal perturbation is applied to an otherwise flat film, and its response is calculated using a linearized version of the differential equation[14]. The resulting dispersion relation quantifies the decay, or amplification, of a given perturbation wavelength with time. The wavelength of the fastest amplified mode is given by:

$$\lambda_m = 2\pi\sqrt{\frac{2\gamma}{\frac{\partial p_{el}}{\partial h}}} \qquad (1)$$

Here p_{el} is a function of the electric field and the dielectric constant of the polymer (Fig. 3). The dotted and dashed lines in Fig. 3 show λ_m as a function of the electric field for slightly different models of the electrostatic pressure p_{el}. A similar equation quantifies the characteristic time τ for the formation of the instability (right-hand axis in Fig. 3). We note that the two curves from equation (1) describe the experimental data well, in the absence of any fitting parameters. Additional data using other polymers, along with a detailed theoretical model, will be discussed elsewhere.

Whereas the topography of the polymer film occurs spontaneously, control of the lateral structure is achieved by laterally varying the electrode spacing d. To this end, the upper electrode is replaced by a topographically patterned master (Fig. 1b). As the electrostatic forces are strongest for smallest electrode spacings d, the time needed for the instability to form is much shorter for smaller values of d (Fig. 3, right hand axis). The emerging structure in the film is therefore focused towards the electrode structure which protrudes downwards towards the polymer film (Fig. 1b). This leads to a replication of the master electrode. Experimental results of this procedure are shown in Fig. 4. We note that the dielectric liquid is drawn up towards the electrode, forming a positive replica, as opposed to the negative patterns achieved by
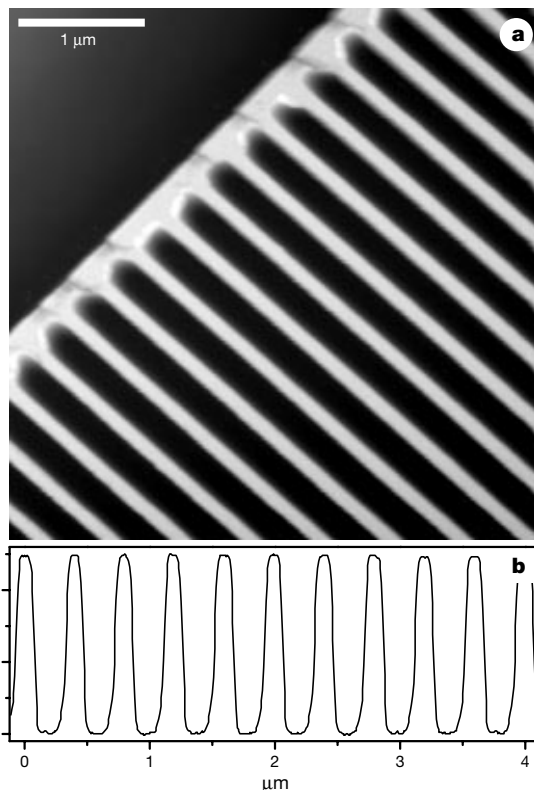
Figure 4 Electrostatic lithography corresponding to the schematic drawing in Fig. 1b. A patterned electrode was mounted facing a brominated polystyrene film ($h \approx 45$ nm). The device was annealed at 170 °C for 14 h. To ensure that no polymer remained on the master electrode after disassembly, the electrode was rendered unpolar by deposition of a self-assembled monolayer. The AFM image (**a**; tapping mode at 360 kHz) shows 140-nm-wide stripes (full-width at half-maximum) which replicate the silicon master electrode (200-nm stripes separated by 200-nm-wide and 170-nm-deep grooves). The cross-section (**b**) reveals a step height of 125 nm. The resolution in **b** is limited by the geometry of the AFM tip. The rounded-off corners at $z = 0$ nm indicate a finite contact angle of the brominated polystyrene on the silicon oxide surface. Apart from this small effect, the profile of the polymer stripes is nearly rectangular, with an aspect ratio of 0.83. The high quality of the replication extends over the entire 100×100 μm^2 area that was covered by the master pattern.

conventional imprinting techniques[2]. Several features of this electrostatic replication process should be pointed out. The quality of the replicated structures is nearly perfect and, to within the resolution of the AFM, the features have perpendicular side walls. The electrostatically induced structure formation in the polymer film is not limited to wavelength around λ_m; rather, a large range in lateral structures can be replicated for otherwise identical experimental parameters. In the example shown here (Fig. 4), lines with a width of 140 nm were reproduced for an average plate spacing of 125 nm and an applied voltage of 42 V: the aspect ratio (height/width) of these structures is ~0.83. The extension to lateral length scales of less than 100 nm and aspect ratios greater than 1 should be possible. We have shown that strong electric field can cause the breakup of dielectric fields, leading to characteristic hexagonal patterns. In combination with a patterned master, this principle can be employed to replicate submicrometre structures. This technique is straightforward, and does not need specialized equipment or specialized chemicals. In a technological application, the spacing between the two electrodes would need to be controlled with great precision, but this could be easily achieved by introducing non-conducting spacers into the capacitor gap. □

1. *The National Technology Roadmap for Semiconductors* (Semiconductor Industry Association Report, 1997).
2. Xia, Y., Rogers, J. A., Paul, K. E. & Whitesides, G. M. Unconventional methods for fabricating and patterning nanostructures. *Chem. Rev.* **99**, 1823–1848 (1999).
3. Landau, L. D., Lifshitz, E. M. & Pitaevski, L. P. *Electrodynamics of Continuous Media* (Pergamon, Oxford, 1984).
4. Amundson, K. *et al.* Effect of an electric field on block copolymer microstructure. *Macromolecules* **24**, 6546–6548 (1991).
5. Amundson, K., Helfand, E., Quan, X. & Smith, S. D. Alignment of lamellar block copolymer microstructure in an electric field. 1. Alignment kinetics. *Macromolecules* **26**, 2698–2703 (1993).
6. Amundson, K., Helfand, E., Quan, X., Hudson, S. D. & Smith, S. D. Alignment of lamellar block copolymer microstructure in an electric field. 2. Mechanisms of alignment. *Macromolecules* **27**, 6559–6570 (1994).
7. Morkved, T. L. *et al.* Local control of microdomain orientation in diblock copolymer thin films with electric fields. *Science* **273**, 931–933 (1996).
8. Thurn-Albrecht, T., DeRouchey, J., Russell, T. P. & Jaeger, H. M. Overcoming interfacial interactions with electric fields. *Macromolecules* (submitted).
9. Blythe, A. R. *Electrical Properties of Polymers* (Cambridge Univ. Press, 1979).
10. Chou, S. Y., Zhuang, L. & Guo, L. Lithographically induced self-construction of polymer microstructures for resistless patterning. *Appl. Phys. Lett.* **75**, 1004–1006 (1999).
11. Chou, S. Y. & Zhuang, L. Lithographically induced self-assembly of periodic polymer micropillar arrays. *J. Vac. Sci. Technol. B* **17**, 3197–3202 (1999).
12. Reiter, G. Dewetting of thin polymer films. *Phys. Rev. Lett.* **68**, 75–78 (1992).
13. de Gennes, P. G. Wetting: statics and dynamics. *Rev. Mod. Phys.* **57**, 827–862 (1985).
14. Herminghaus, S. Dynamical instability of thin liquid films between conducting media. *Phys. Rev. Lett.* **83**, 2359–2361 (1999).

•••

Variations of Younger Dryas atmospheric radiocarbon explicable without ocean circulation changes

Tomasz Goslar*, Maurice Arnold†, Nadine Tisnerat-Laborde†, Justyna Czernik* & Kazimierz Więckowski‡

* *Institute of Physics, Silesian Technical University, 44-100 Gliwice, Poland*
† *Laboratoire des Sciences du Climat et de l'Environnement, CNRS-CEA, 91198 Gif sur Yvette, France*
‡ *Institute of Geography and Spatial Organization, Polish Academy of Sciences, 00-325 Warsaw, Poland*

....

The concentration of radiocarbon, ^{14}C, in the atmosphere depends on its production rate by cosmic rays, and on the intensity of carbon exchange between the atmosphere and other reservoirs, for example the deep oceans. For the Holocene (the past ~11,500 years), it has been shown that fluctuations in atmospheric radiocarbon concentrations have been caused mostly by variations in the solar magnetic field[1-3]. Recent progress in extending the radiocarbon record backwards in time[4-10] has indicated especially high atmospheric radiocarbon concentrations in the Younger Dryas cold period, between 12,700 and 11,500 years before the present. These high concentrations have been interpreted as a result of a reduced exchange with the deep-ocean reservoir, caused by a drastic weakening of the deep-ocean ventilation[7-9,11,12]. Here
we present a high-resolution reconstruction of atmospheric radiocarbon concentrations, derived from annually laminated sediments of two Polish lakes, Lake Gościąż and Lake Perespilno. These records indicate that the maximum in atmospheric radiocarbon concentrations in the early Younger Dryas was smaller than previously believed, and might have been caused by variations in solar activity. If so, there is no indication that the deep-ocean ventilation in the Younger Dryas was significantly different from today's.

The basic set of data consists of ^{14}C dates of the varved sediments of Lake Gościąż (LG). The LG dates published so far[7] covered densely the time span between 11,800–10,500 calendar years before present, but only a few dates from before 11,800 cal. yr BP were available. In this work, we sampled the oldest part of the LG sediments, that is, between 12,950 and 11,700 cal. yr BP.

An additional data set comes from Lake Perespilno (LP), in eastern Poland. The sediments of that lake[13] contain 3,100 varves in two sections. The younger one, covering the Younger Dryas, has been synchronized with the LG timescale, using the ^{14}C dates and pollen analysis[13]. Here, we completed ^{14}C measurements of the older section, and dated it to 14,455–13,645 ($\pm$50) cal. yr BP, by matching the LP ^{14}C dates to the coral ^{14}C calibration data[4-6]. The calendar and ^{14}C ages from Lakes Gościąż and Perespilno are provided in the Supplementary Information.

The LG dates (Fig. 1) perfectly match the high-precision ^{14}C calibration curve of German pines (GP; ref. 14), except for the oldest end of that curve. This would imply more than 200 varves missing from the LG chronology before 11.6 kyr BP, which is highly improbable as the chronology is replicated in many cores from three separate lake basins. Alternatively, the discrepancy might reflect problems with cross-correlation of the pine tree-ring sequences in that period, when few trunks are available, the tree-rings are very thin, and are frequently even missing[15].

Except for a few outliers, the LG dates agree well with those obtained on corals[4-6,16] and on the sediments of Lake Suigetsu (LS), Japan[10]. However, ^{14}C dates from the Cariaco Basin, Atlantic[9], in the period between 13 and 12.5 kyr BP are significantly younger. This seems to be connected with the large difference between absolute ages of the Alleröd/Younger Dryas boundary in both archives (Fig. 2 and inset to Fig. 1). In all probability, one of two chronologies (either Cariaco or LG) has some error around the mid-Younger Dryas.

The ages of both Alleröd/Younger Dryas and Younger Dryas/Holocene boundaries in LG (ref. 8) perfectly agree with those estimated in the GRIP ice core[17,18]. On the other hand, the chronology of the Cariaco sediments seems to be supported by that of the GISP2 ice core[19]. Direct comparison of proxy climatic records shows distinct time lags between several events (Fig. 2) recorded in both Greenland ice cores. This implies that either the GRIP or GISP2 chronology needs adjustment.

There are arguments for the correctness of the GRIP and LG time scales. The duration of the Younger Dryas in LG agrees very well with that in LP (ref. 13), and in the revised chronologies of German Maar lakes[20]. ^{14}C dates of the oldest samples from LG (around 12.9 kyr BP) fitted most of the dates from corals and from the Lake Suigetsu, whereas in the same period, all the Cariaco dates are younger. Additionally, they offset the coral and LS dates in the whole preceding millennium. These arguments suggest that the Cariaco (and GISP2) timescales may not be adequate. Indeed, the ^{10}Be record from GISP2 (ref. 21) between 8 and 5 kyr BP, lags the dendro-dated record of atmospheric ^{14}C concentration by about 100 years, which is difficult to explain unless there is an error in GISP2 chronology[3]. In fact, the Younger Dryas/Holocene transitions in Cariaco and GISP2 are about 100 years older than in the GRIP, LG and GP archives.

The LG and LP data points (Fig. 1) have been connected by a spline curve. We realised that combining data from archives that are

877